

Supporting Information:

Dissociative chemisorption of O₂ on Al(111): Dynamics on a potential energy surface computed with a non- self-consistent screened hybrid density functional approach

Robert A. B. van Bree^{,†}, Nick Gerrits[†], and Geert-Jan Kroes^{*,†}*

[†] Leiden Institute of Chemistry, Leiden University, Gorlaeus Laboratories, P.O.

Box 9502 2300 RA Leiden, the Netherlands

Email: r.a.b.van.bree@lic.leidenuniv.nl, g.j.kroes@chem.leidenuniv.nl

Table of contents

| | |
|---|----|
| S1 Supporting information | 3 |
| S1.1 Coordinate system and dynamical model..... | 3 |
| S1.2 Density functionals..... | 3 |
| S1.3 Construction of the PESs. | 5 |
| S1.4 Quasi-classical trajectory calculation. | 6 |
| S1.5 Hole model..... | 8 |
| S2 Supporting Figures | 10 |
| S2.1 Figure S1..... | 10 |
| S2.2 Figure S2..... | 11 |
| S2.3 Figure S3..... | 12 |
| S3 Supporting Tables | 13 |
| S3.1 Table S1..... | 13 |
| S3.2 Table S2..... | 14 |
| S4 References | 15 |

S1 Supporting information

S1.1 Coordinate system and dynamical model.

The coordinate system used in this work is as used in previous work on diatomic molecules reacting on (111) surfaces of fcc metals, see ref:¹ for a detailed account. For the dynamics calculations in this paper, we make use of the Born-Oppenheimer static surface (BOSS) approximation, which means that we employ both the Born-Oppenheimer approximation (BOA) and keep all Al(111) surface atoms fixed in their ideal lattice position². This way, we only have to consider the six degrees of freedom associated with the diatomic molecule (O_2). Therefore, we can use the molecule's centre-of-mass (COM) centralized coordinate system for the molecule's degrees of freedom. In this coordinate system, the COM's position is expressed in the coordinates X and Y for motion along the surface, and Z is the distance of the molecule's COM to the surface. The distance between the oxygen atoms is given by the r coordinate. The azimuthal angle φ defines the orientation of the molecule's projection on the surface, i.e., on the horizontal- (X, Y) -plane, and the polar angle θ defines the angle of the O_2 bond axis with the Z -axis. For a visual representation see **Figure S1A**.

The surface unit cell of a (111) surface of an FCC metal is illustrated in **Figure S1B**. In this figure, the most relevant high-symmetry sites are also indicated. Note that the angle between the U and V axes can be taken as either 60 or 120 degrees; in **Figure S1B** the 60-degree version is demonstrated. As we are describing a unit cell, the U and V coordinates within this cell are taken as normalized (between 0 and 1). The X and Y coordinates of the COM of O_2 are transformed to U, V -space to properly describe the position of the COM of O_2 above a (111) FCC surface and its high symmetry sites.

S1.2 Density functionals.

The density functionals used in this work are the RPBE³ DF at the generalized gradient approximation (GGA) rung and the HSE03-1/3x DF⁴ at the screened hybrid rung of DFT. The RPBE DF may be viewed³

as a variant of the non-empirical GGA PBE DF⁵, with the RPBE DF originally designed to improve the description of chemisorption energies of atoms and molecules on metal surfaces. Hammer *et. al.* constructed the RPBE DF in such a way that the same non-empirical constraints imposed on the PBE-DF are also imposed on RPBE³. Importantly for metals, the recovery of the uniform electron gas limit at zero gradient of the density is included⁶. In general, we can consider the RPBE functional as more ‘repulsive’ than the PBE functional, i.e., the RPBE barriers for both gas phase reactions and dissociative chemisorption reactions on metals are higher than the PBE DF barriers^{7,8}. This results in lower reactivity when describing a gas-metal system with the RPBE functional².

The HSE03-1/3x DF is a screened hybrid functional. It is a hybrid DF because a fraction of exact exchange (also somewhat ambiguously called Hartree-Fock exchange) is admixed to the GGA exchange⁹. It is screened because the exact exchange is turned off at long range. This means that at long range the functional behaves like a PBE DF⁵, whereas at short range it will behave as a PBE0-like hybrid DF¹⁰. The screening of the exact exchange in metals is vital, because without it a myriad of descriptive issues can occur, not the least of which is a reduction of the density of states of the electrons at the Fermi level¹¹.

The HSE03-1/3x DF is similar to the original HSE03 DF^{4,12}, i.e., to the HSE03 DF that has been corrected for an implementation error¹². The HSE03 DF only differs from the better-known HSE06 functional through the use of a slightly different screening range parameter^{4,12}. The difference between the HSE03-1/3x DF and the HSE03 DF in ref. ⁴ is that we implemented a different maximum fraction of exact exchange (α). The α -values for PBE0 and HSE03 were originally set to 1/4, whereas we use α 1/3. Increasing the exact exchange is an accepted approach to improve the performance for gas phase reaction barrier heights^{13,14}, and was thus used already in earlier work on O₂ + Al(111)¹⁵ to improve over the description of the O₂ on Al(111) system obtained with the original HSE03 functional.

Here a non-self-consistent field (NSCF) HSE03-1/3x@RPBE calculation is performed by first initializing and converging a self-consistent field (SCF) calculation with the lower level RPBE functional to obtain a well-converged electron density. The higher level HSE03-1/3x density functional⁴ is then applied once to this density (using its Kohn-Sham wavefunction) to compute the HSE03-1/3x@RPBE energy. Vital to achieving an accurate and converged result in this type of calculation is that a high enough level of convergence is achieved for the energy (and thereby the density) at the lower (RPBE) level of theory. We have found that this requires a tougher energy tolerance than usually needed in a self-consistent calculation, presumably because the RPBE density is not equal to the density that corresponds to the variational minimum energy that would be obtained with the self-consistent HSE03-1/3X functional.

S1.3 Construction of the PESs.

In the most common approach to performing quasi-classical trajectory (QCT) dynamics calculations a continuous and global PES is used that is fitted to electronic structure calculations using the DF of which the accuracy is evaluated. As discussed in section S1.1 of this SI, the PES in this work is dependent on the six degrees of freedom of the diatomic (O_2) molecule. A continuous representation of this six-dimensional PES is obtained by applying the corrugation-reducing procedure (CRP)^{16,17} to a grid of DFT single-point energies. In this approach, atom-surface PESs are subtracted from the full 6D PES such that the remaining PES is less corrugated and easier to interpolate. In previous studies this procedure led to off-grid interpolation errors that were no larger than 30 meV¹⁷ (2.9 kJ/mol) and 0.7 kcal/mol¹⁸ (2.9 kJ/mol). Moreover, in the work of Smeets *et. al.* a large test set of 4900 samples was used to test the interpolation error of the CRP method¹⁹. This resulted in a root mean squared error (RMSE) of 31 meV (3.0 kJ/mol). However, this RMSE was reduced to 8 meV (0.8 kJ/mol) if the interaction energies between molecule and metal were smaller than 4 eV¹⁹. For $O_2+Al(111)$, most interaction energies are within 4 eV in the configuration space relevant to the reaction dynamics (see also **Figure 6**). Furthermore, **Table S2** shows a comparison of reaction barrier energies extracted from the CRP PES (as also shown in **Table 1**) with values directly calculated for the corresponding CRP barrier geometries

using DFT (the NSCF HSE03-1/3x@RPBE DF). The RMSE of 0.61 kJ/mol is consistent with the value of 0.8 kJ/mol for total interaction energies smaller than 4 eV in the earlier cited study, with the largest deviation between a CRP and a DFT barrier being about 3.0 kJ/mol, in what is a clear outlier in the set. The CRP procedure used in this work is along similar lines as in e.g. the work of Ref.²⁰, except for two distinctions.

First, we did not employ an equidistant (r, Z) -grid. Instead, we used a similar grid as used in ref.¹⁵ for the calculations with the SCF HSE03-1/3x functional, i.e., $Z = [1.00, 1.50, 2.00, 2.25, 2.50, 2.75, 3.00, 3.25, 3.50] \text{ \AA}$, and $r = [1.0, 1.1, 1.15, 1.175, 1.2, 1.225, 1.25, 1.3, 1.4, 1.5, 1.6] \text{ \AA}$. This grid limits the number of single points necessary for a good representation whilst maintaining high accuracy for the description of the molecule in the gas phase and at the TS. We opted to use the same grid as the earlier $\text{O}_2 + \text{Al}(111)$ work of Gerrits *et. al.* to enable an optimal comparison with the calculations using the SCF HSE03-1/3x DF PES, in the sense that differences should not be attributable to the use of a different grid of points.

The second distinction is that similar to reference¹⁵, we employ the atomic 3D PES computed with the MS-RPBE DF²¹ instead of an atomic PES obtained with the (NSCF) HSE03-1/3x functional. This is done to maintain comparative PESs between the NSCF and SCF DF. Regardless, the three-dimensional atomic PES will not influence the 6D PES itself as long as the 3D potential is physically reasonable, since the 3D atomic PES is used only to decrease the corrugation of the 6D PES during the fitting procedure, as also discussed in Ref.¹⁵.

S1.4 Quasi-classical trajectory calculation.

A global PES as produced by the CRP allows for performing quasi-classical trajectory (QCT)^{22,23} dynamics calculations, along similar lines as in previous work^{15,19,24}. With QCT we take into account the molecule's initial zero-point energy, after which the molecular trajectory is propagated classically in

time. If the bond length of O₂ exceeds the threshold of 1.59 Å in a trajectory, we count that trajectory as reacted. If the value of Z increases beyond the value of Z at the starting point of the trajectory (i.e., if $Z > 5.0 \text{ \AA}$) we consider the molecule to be scattered. The reaction probability (P_r) is calculated using:

$$P_r = \frac{N_r}{N_{total}} \quad (S1)$$

where N_r is the number of trajectories that correspond to reaction and N_{total} is the total number of the trajectories run.

Two types of molecular beams were simulated for this work. This first type is used to simulate the experiments of Österlund *et. al.*²⁵, for which supersonic molecular beams with a nozzle temperature (T_N) equal to room temperature, i.e., 300 K, were used. In simulating the experiments the vibrational temperature of the molecules can be taken equal to the value of T_N in the experiments²⁵. Due to the high rotational cooling in the oxygen molecular beams employed, the rotational temperature of O₂ is only 9K²⁶, resulting in a rovibrational state population presented in **Table S1** (see Refs.^{19,27} for more information). In the QCT calculations, we used a single value for the incidence energy of the molecule and allowed initial states with $v = 0 - 3$, and $j = 1 - 49$ to be populated. However, **Table S1** shows that O₂ molecules in a beam with $T_N = 300$ K mostly occupy the rovibrational ground state ($v=0, j=1$). Note that we only consider the odd j states, because the even j states are forbidden according to nuclear spin statistics. For this beam simulation, we ran 10,000 trajectories for each incidence energy to compute the reaction probability (P_r) per incidence energy with converged statistics.

The second type of beam is used to simulate the experiments of Kurahashi and Yamauchi²⁸, for which we employed a state-specific initial condition of $v=0, j=1$, with appropriate averaging over $m_j = -1, 0, 1$, according to the particular experiment simulated. We ran 2800 trajectories per incidence energy to compute the sticking probability. We then use the m_j state-specific reaction probabilities and the

equations provided in the work of Kurahashi and Yamauchi²⁸ to compute the reaction probabilities measured for particular rotational alignments. We refer the reader to reference²⁸ for the details.

S1.5 Hole model

The hole model²⁹ is a method to study the barrier corrugation and anisotropy without the usage of dynamics². For this work we used the well-defined NSCF PES to compute the reaction, or sticking, probability, as described by the hole model^{2,29}:

$$S_0(E_{mol}) = \int H\{E_{mol} - E_B(X, Y, \theta, \varphi)\} dX dY d\cos(\theta) d\varphi \quad (S2)$$

$$H\{\Delta E\} = \begin{cases} 1 & \text{if } \Delta E \geq 0 \\ 0 & \text{if } \Delta E < 0 \end{cases} \quad (S3)$$

Here E_{mol} is the sum of the internal energy of the molecule (as defined by the temperature of the molecular beam) and the incidence energy of the molecule, and $E_B(X, Y, \theta, \varphi)$ is the energy of the barrier for a given molecular geometry (X, Y, θ, φ) .

In practice, we opt to use a Monte-Carlo-like approach to solving this integral. Where analogous to section S1.4, we compute the reaction probability as equation S1, though now we do not use quasi-classical trajectory outcomes but distinct samples such that:

$$P_r(E_I) = \frac{N_r(E_I)}{N_{total}} = \frac{\sum_j^{N_{total}} H\{E_j^{mol}(E_I) - E_j^B(U_j, V_j, \cos(\theta)_j, \varphi_j)\}}{N_{total}} \quad (S4)$$

$$E_j^{mol}(E_I) = E_I + E_j^{vibration} + E_j^{rotation} \quad (S5)$$

where E_I is the incidence energy of the molecule, $E^{vibration}$ and $E^{rotation}$ are the vibration energy and rotation energy of the molecule for each sample j chosen randomly via the $T_N = 300K O_2$ molecular beam population distribution (see also table S1), N_{total} is the total number of samples used, H is the same Heaviside function as in equation S3, and $U, V, \cos(\theta), \varphi$ are chosen uniformly random for each j and are defined as in section S1.1 (Note that in equations S4 we use the U, V coordinates instead of

X, Y see also section S1.1). If N_{total} is chosen to be large enough (in this work it is chosen to be 10^6) equation S4 should approach the results of equation S2.

For each sample j , a molecular energy and molecular geometry (U, V, θ, φ) are thus chosen according to the same initial conditions as in the QCT calculations. The geometry is used to compute the reaction barrier in r and Z via a simple two-dimensional barrier searching algorithm applied to the (NSCF) PES. The barrier search is in principle a basic saddle-point searching algorithm, assuming that only one saddle-point, or barrier, will exist per r, Z -elbow cut of the PES. The saddle points are found by starting a modified Powell method^{30,31} root finding algorithm on the Jacobian of the two-dimensional (r, Z) PES from an initial guess on the elbow. This critical point is then verified to be a saddle point via a second order derivative test with the hessian of the two-dimensional (r, Z) PES on the critical point (i.e., the discriminant of the hessian needs to be smaller than zero) if the critical point is not a saddle point, a new root search in the Jacobian is started from a different initial guess. This algorithm is basic but robust if the corrugation of the PES is reduced as much as possible (to avoid the occurrence of false critical or even saddle points).

S2 Supporting Figures

S2.1 Figure S1

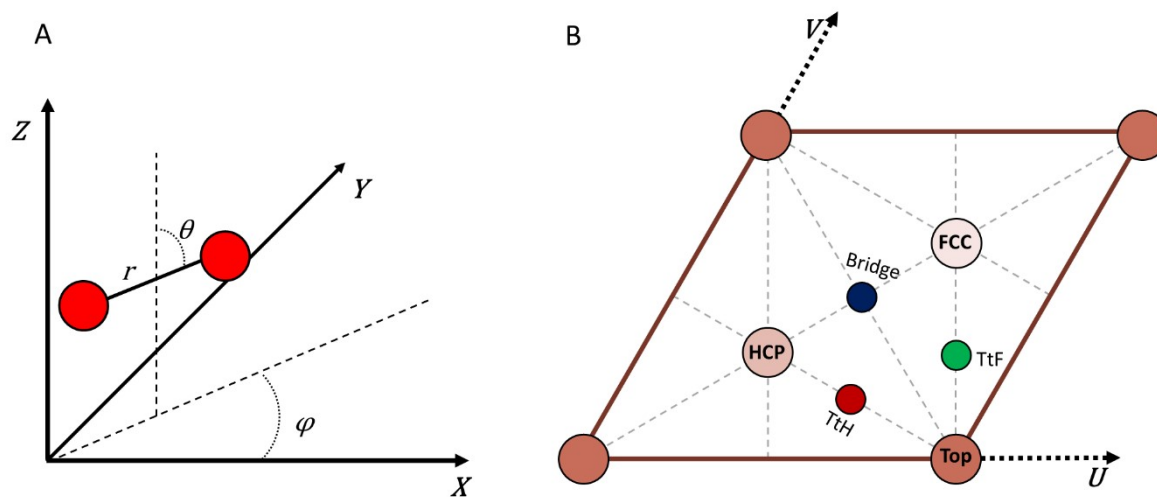


Figure S1: The coordinate system in use and its relation with the Al(111) surface unit cell. **A:** The centre-of-mass coordinate system used for the description of O_2 interacting with Al(111). See the text in Section S1.1 for an explanation of the coordinates shown. **B:** The unit cell of a (111) surface of an FCC metal (Al), in which the high symmetry surface sites are indicated.

S2.2 Figure S2

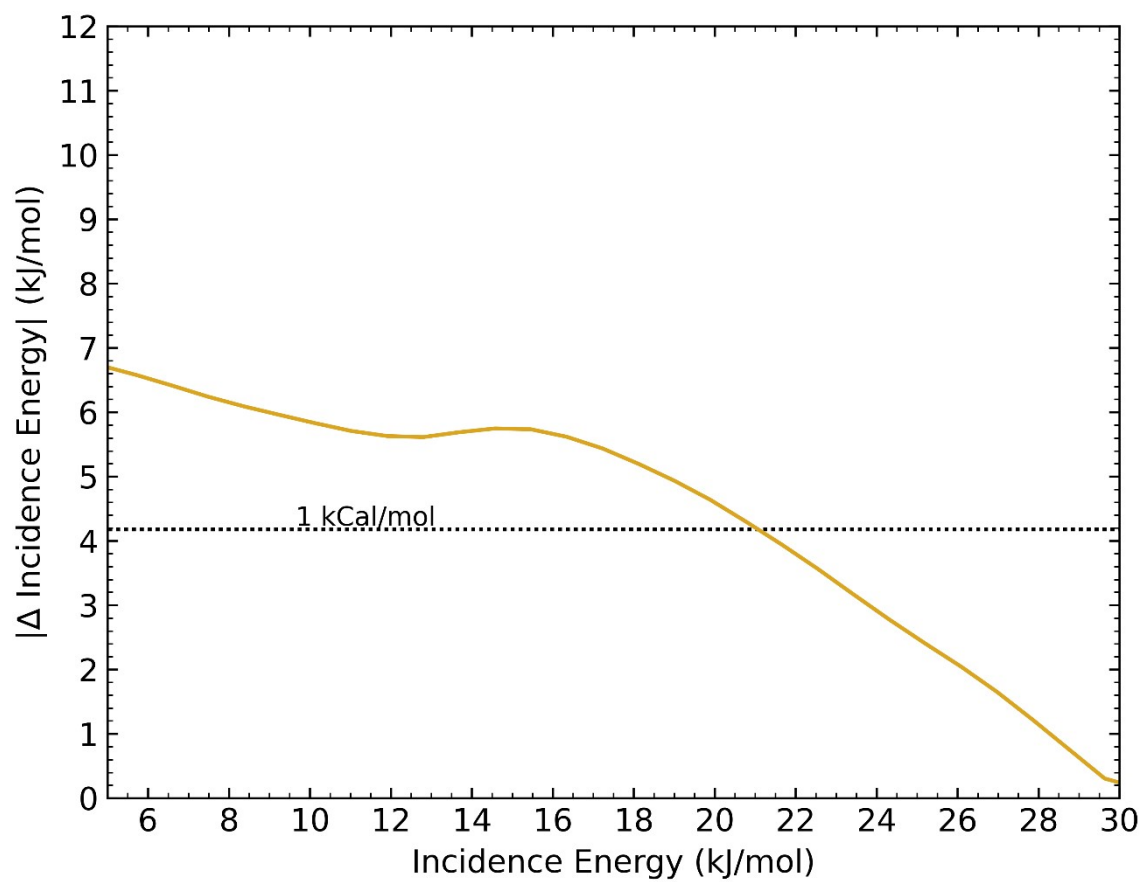


Figure S2: The absolute difference of incidence energy between the hole model reaction probability and the QCT reaction probability as a function of the incidence energy of the Hole model, moving the reaction probability curves in Figure 7 from left (hole model) to right(QCT).

S2.3 Figure S3

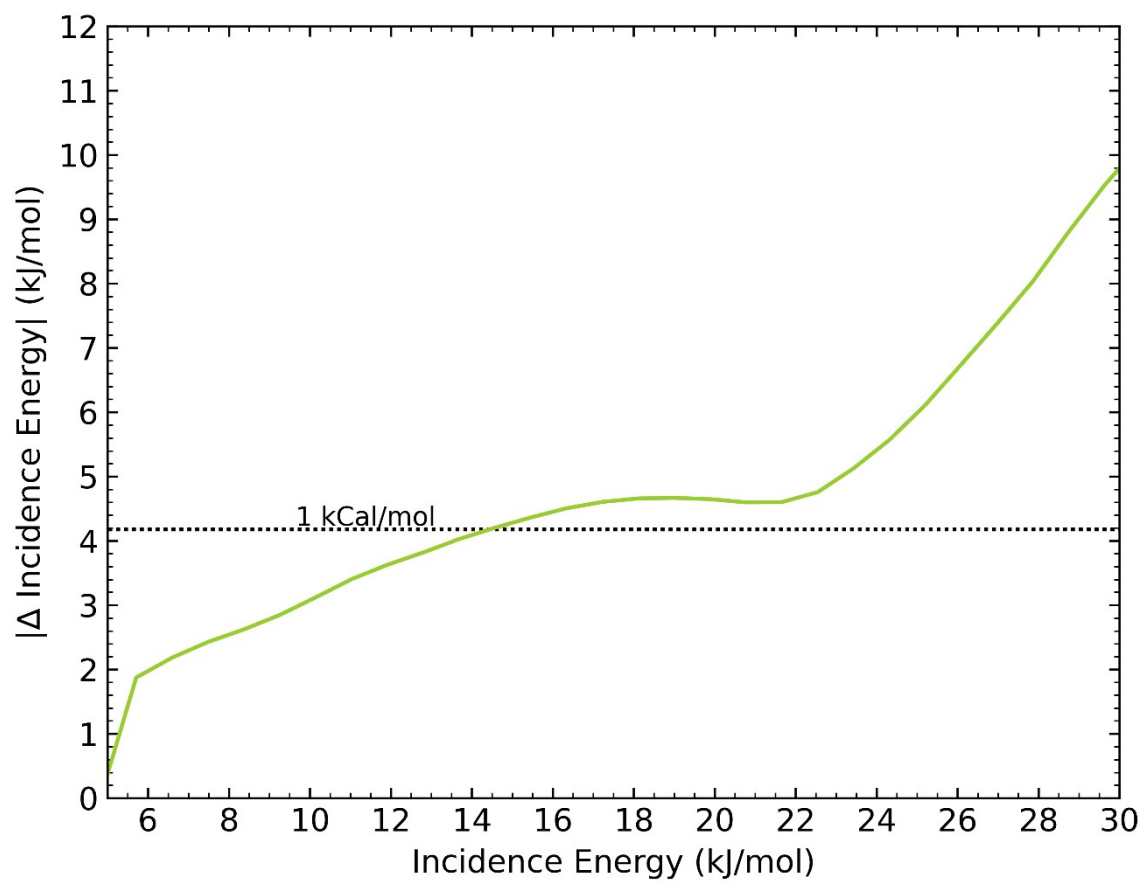


Figure S3: The absolute difference of incidence energy between the QCT reaction probability and the reaction probability of the hole model excluding vibrational energies as a function of the incidence energy of the QCT, moving the reaction probability curves in Figure 7 from left(QCT) to right (hole model Excl. Vibrations).

S3 Supporting Tables

S3.1 Table S1

Table S1: Rovibrational state population in an O_2 molecular beam with a nozzle temperature of 300 K.

| ν state | j state | Rovibrational energy (eV) | Population |
|-------------|-----------|---------------------------|------------|
| 0 | 1 | 0.10687 | 80.6546 % |
| 0 | 3 | 0.10865 | 18.8495 % |
| 0 | 5 | 0.11186 | 0.47049 % |
| 0 | 7 | 0.11650 | 0.00160 % |
| 1 | 1 | 0.31449 | 0.02632 % |
| 1 | 3 | 0.31626 | 0.00627 % |
| 1 | 5 | 0.31944 | 0.00016 % |

S3.2 Table S2

Table S2: Barrier energies as extracted from the CRP PES, and computed with DFT single point calculations for the CRP barrier geometries, the deviation (Δ) between them, and the resulting root mean squared error based on the deviations. See Figure S1B for the name and location of the high symmetry sites; the O_2 orientation is indicated with P(parallel) for $\theta=90^\circ$, N(Normal) for $\theta=0^\circ$, and T(Tilted) for $\theta=45^\circ$.

| High Symmetry geometry | CRP HSE03-1/3x@RPBE Barrier height (kJ/mol) | DFT HSE03-1/3x@RPBE Barrier height (kJ/mol) | Δ (DFT-CRP) Barrier height (kJ/mol) |
|-------------------------------|---|---|--|
| Top N | 29.833 | 29.735 | -0.098 |
| Top P, $\varphi: 0^\circ$ | 24.423 | 24.152 | -0.271 |
| Top P, $\varphi: 30^\circ$ | 24.409 | 24.189 | -0.220 |
| Bridge N | 25.451 | 25.334 | -0.117 |
| Bridge P, $\varphi: 0^\circ$ | 6.559 | 6.533 | -0.027 |
| Bridge P, $\varphi: 60^\circ$ | 29.727 | 29.470 | -0.257 |
| Bridge P, $\varphi: 90^\circ$ | 51.360 | 54.332 | 2.972 |
| TtF N | 29.108 | 29.127 | 0.019 |
| TtF T, $\varphi: 150^\circ$ | 37.979 | 37.285 | -0.694 |
| TtF T, $\varphi: 240^\circ$ | 16.688 | 16.686 | -0.003 |
| TtF T, $\varphi: 330^\circ$ | 16.625 | 16.625 | 0.000 |
| TtF P, $\varphi: 240^\circ$ | 28.736 | 28.527 | -0.209 |
| TtF P, $\varphi: 330^\circ$ | 12.835 | 12.624 | -0.212 |
| TtH N | 27.718 | 27.690 | -0.028 |
| TtH T, $\varphi: 30^\circ$ | 16.821 | 16.832 | 0.011 |
| TtH T, $\varphi: 120^\circ$ | 16.920 | 16.930 | 0.009 |
| TtH T, $\varphi: 210^\circ$ | 36.335 | 35.837 | -0.498 |
| TtH P, $\varphi: 30^\circ$ | 12.313 | 12.031 | -0.282 |
| TtH P, $\varphi: 120^\circ$ | 37.847 | 37.466 | -0.381 |
| FCC N | 38.521 | 38.982 | 0.460 |
| FCC T, $\varphi: 150^\circ$ | 32.487 | 32.623 | 0.136 |
| FCC T, $\varphi: 330^\circ$ | 60.026 | 59.569 | -0.457 |
| FCC P, $\varphi: 0^\circ$ | 13.507 | 13.218 | -0.289 |
| FCC P, $\varphi: 330^\circ$ | 14.612 | 14.289 | -0.332 |
| HCP N | 34.616 | 34.929 | 0.313 |
| HCP T, $\varphi: 210^\circ$ | 30.969 | 31.125 | 0.156 |
| HCP T, $\varphi: 30^\circ$ | 56.217 | 56.139 | -0.078 |
| HCP P, $\varphi: 0^\circ$ | 12.707 | 12.455 | -0.252 |
| HCP P, $\varphi: 30^\circ$ | 13.700 | 13.551 | -0.149 |
| RMSE | - | - | 0.614 |

S4 References

- 1 G.-J. Kroes and C. Díaz, *Chem. Soc. Rev.*, 2016, **45**, 3658–3700.
- 2 G.-J. Kroes, *Phys. Chem. Chem. Phys.*, 2021, **23**, 8962–9048.
- 3 B. Hammer, L. B. Hansen and J. K. Nørskov, *Phys. Rev. B*, 1999, **59**, 7413–7421.
- 4 J. Heyd, G. E. Scuseria and M. Ernzerhof, *J. Chem. Phys.*, 2003, **118**, 8207–8215.
- 5 J. P. Perdew, K. Burke and M. Ernzerhof, *Phys. Rev. Lett.*, 1996, **77**, 3865–3868.
- 6 J. P. Perdew, A. Ruzsinszky, J. Tao, V. N. Staroverov, G. E. Scuseria and G. I. Csonka, *J. Chem. Phys.*, 2005, **123**, 062201.
- 7 C. Díaz, E. Pijper, R. A. Olsen, H. F. Busnengo, D. J. Auerbach and G. J. Kroes, *Science (80-.)*, 2009, **326**, 832–834.
- 8 M. Wijzenbroek and G. J. Kroes, *J. Chem. Phys.*, , DOI:10.1063/1.4865946.
- 9 J. P. Perdew, M. Ernzerhof and K. Burke, *J. Chem. Phys.*, 1996, **105**, 9982–9985.
- 10 C. Adamo and V. Barone, *J. Chem. Phys.*, 1999, **110**, 6158–6170.
- 11 W. Gao, T. A. Abtew, T. Cai, Y. Y. Sun, S. Zhang and P. Zhang, *Solid State Commun.*, 2016, **234–235**, 10–13.
- 12 J. Heyd, G. E. Scuseria and M. Ernzerhof, *J. Chem. Phys.*, 2006, **124**, 219906.
- 13 N. Mardirossian and M. Head-Gordon, *Mol. Phys.*, 2017, **115**, 2315–2372.
- 14 A. J. Cohen, P. Mori-Sánchez and W. Yang, *Chem. Rev.*, 2012, **112**, 289–320.
- 15 N. Gerrits, E. W. F. Smeets, S. Vuckovic, A. D. Powell, K. Doblhoff-Dier and G.-J. Kroes, *J. Phys. Chem. Lett.*, 2020, **11**, 10552–10560.
- 16 H. F. Busnengo, A. Salin and W. Dong, *J. Chem. Phys.*, 2000, **112**, 7641–7651.
- 17 R. A. Olsen, H. F. Busnengo, A. Salin, M. F. Somers, G. J. Kroes and E. J. Baerends, *J. Chem. Phys.*, 2002, **116**, 3841–3855.
- 18 A. D. Powell, N. Gerrits, T. Tchakoua, M. F. Somers, H. F. Busnengo, J. Meyer, G. Kroes and K. Doblhoff-Dier, *J. Phys. Chem. Lett.*, 2024, 307–315.
- 19 E. W. F. Smeets and G. J. Kroes, *J. Phys. Chem. C*, 2021, **125**, 8993–9010.

- 20 M. Wijzenbroek, D. M. Klein, B. Smits, M. F. Somers and G. J. Kroes, *J. Phys. Chem. A*, 2015, **119**, 12146–12158.
- 21 E. W. F. Smeets, J. Voss and G.-J. Kroes, *J. Phys. Chem. A*, 2019, **123**, 5395–5406.
- 22 L. M. Raff and M. Karplus, *J. Chem. Phys.*, 1966, **44**, 1212–1229.
- 23 M. Karplus, R. N. Porter and R. D. Sharma, *J. Chem. Phys.*, 1965, **43**, 3259–3287.
- 24 N. Gerrits, J. Geweke, E. W. F. Smeets, J. Voss, A. M. Wodtke and G.-J. Kroes, *J. Phys. Chem. C*, 2020, **124**, 15944–15960.
- 25 L. Österlund, I. Zoric-acute and B. Kasemo, *Phys. Rev. B*, 1997, **55**, 15452–15455.
- 26 N. A. Kuebler, M. B. Robin, J. J. Yang, A. Gedanken and D. R. Herrick, *Phys. Rev. A*, 1988, **38**, 737–749.
- 27 G. Füchsel, M. Del Cueto, C. Díaz and G. J. Kroes, *J. Phys. Chem. C*, 2016, **120**, 25760–25779.
- 28 M. Kurahashi and Y. Yamauchi, *Phys. Rev. Lett.*, 2013, **110**, 246102.
- 29 M. Karikorpi, S. Holloway, N. Henriksen and J. K. Nørskov, *Surf. Sci. Lett.*, 1987, **179**, L41–L48.
- 30 M. J. Powell, *Numerical methods for nonlinear algebraic equations*, Gordon and Breach, New York, 1970.
- 31 B. S. Garbow, K. E. Hillstorn and J. J. More, 1980.